

Experimentally Mapping the Phase Diagrams of Photoexcited Small Polarons

Jocelyn L. Mendes and Scott K. Cushing*

Division of Chemistry and Chemical Engineering, California Institute of Technology, Pasadena,
California 91125, United States

*Correspondence and requests for materials should be addressed to S.K.C. (email: scushing@caltech.edu)

Abstract

Understanding the fundamental properties that dictate photoexcited polarons in materials is critical to tuning their properties. Theoretical models of polarons have only recently been extended to the excited state. Experimental measurements of polaron formation and transport have been widely undertaken across a range of materials, from photocatalysts and superconductors to soft conducting polymers. Here, we map experimental measurements of quantities such as polaron strength onto phase diagrams of the Holstein, Hubbard–Holstein, and t-J–Holstein models. This work demonstrates that tuning electron–phonon coupling strength, electron localization, and spin exchange can be leveraged to suppress or control polaron formation in transition metal oxides. We find that the t-J–Holstein model best describes the measured iron oxides and could be generally applied to a wide range of systems that exhibit polaron formation in the excited state. This work combines experimental data with ground state models to provide a robust parameter space for informing photoexcited polaron design.

Introduction

Polarons dominate material physics, ranging from solar energy materials,¹ O-LEDs,² organic semiconductors,³ conducting polymers,⁴ and even superconductors.⁵ A polaron is the localization of a charge carrier due to coupling with local lattice deformations. The extent of the charge carrier’s localization results in a distinction between small and large polarons, but this definition is often ambiguous.⁶ It is generally accepted that a small polaron is localized to a unit cell or less in a strong coupling perturbation limit, while large polarons span multiple unit cells; however, the crossover between small and large polarons is an active area of study.^{6,7} Extensive work has been undertaken both experimentally and computationally to understand and model polaronic behavior in emergent materials, ranging from scanning probe microscopy and core-level spectroscopy to numerical solutions of the Holstein model, which describes polaronic mobility.^{8–12} Small polarons have been measured and theoretically described in the ground state for decades.^{13–16} Here, we focus on understanding the fundamental properties of *photoexcited* polarons in solid-state materials, an area that remains less understood, despite a range of measurements of individual systems.

Photoexcited polarons form when a charge transfer transition redistributes the charge density between two local orbitals and the carriers couple to lattice vibrations. For example, in a transition metal oxide that is a charge transfer insulator, photoexcitation transfers an electron from a dispersive O 2p orbital to a localized transition metal d-orbital. Usually, during the photoexcited carrier thermalization time, the polarizable lattice of the transition-metal oxide locally distorts, trapping the charge carrier. This has been widely studied in the candidate photoelectrode hematite ($\alpha\text{-Fe}_2\text{O}_3$), showing that small-polaron formation occurs within <100 fs during the first electron-optical-phonon scattering event.^{10,17,18} Polaron localization reduces carrier mobility and photoconversion efficiency, limiting the solar energy and fuel applications of hematite despite its otherwise favorable energetic properties.

Since initial measurements on $\alpha\text{-Fe}_2\text{O}_3$, a wide range of transition metal oxides have been measured to modify, understand, and suppress small polaron formation in strongly polar semiconductors.^{17–21} Altering

the nature of the local lattice, the metal center, surface functionalization, and spin correlations has reduced the strength and even suppressed small polarons in this class of materials. However, succinct design rules that can be used to predict new materials or extend ground state small polaron properties to the excited state have yet to be realized.

Here, we map a range of experimental photoexcited small polaron measurements in transition metal oxides onto three ground-state models: the Holstein, Hubbard–Holstein, and t-J–Holstein Hamiltonians. The resulting phase diagrams are constructed using ultrafast X-ray spectroscopy techniques that measure formation energy, phonon energy, and formation rate, which can be used to approximate the polaron binding energy and electron–phonon coupling strength, supplemented by known exchange energies per spin in literature. We focus particularly on iron oxide systems to standardize metal centers for comparison of the results. Additionally, we consider only measurements of electron polarons on metal centers within these transition metal oxides, due largely to the fact that more X-ray spectroscopy-based measurements of electron polarons exist in the literature. While hole polarons are likely also forming on ligand sites during the photoexcited polaron formation process in these materials, it is challenging to measure both simultaneously. We demonstrate that commonly employed scaling factors for polaron mobility and strength remain valid in the excited state. The Holstein model effectively maps excited state dynamics onto the small-to-large polaron transition but provides limited insight beyond the role of the electron–phonon coupling strength. The Hubbard–Holstein model accounts for on-site repulsion (U) and well describes the small-to-large polaron transition, but it predicts bipolaron regimes that are rarely observed experimentally in the systems considered here. The t-J–Holstein model, related to the Hubbard–Holstein model in the strong coupling limit, provides the most insight by accurately describing when superexchange competes with electron–phonon coupling to reduce polaron localization in the excited state. These findings highlight that on-site electron-spin correlations are critical design parameters for controlling polarons in the photoexcited state. The resulting phase diagram parameterizations provide an applicable excited-state descriptor not only for solid-state systems but also molecular semiconductors,²² and therefore we expect it to find wide use across solar energy materials,²³ soft conducting polymers,²⁴ and even insight into correlated quantum phases like superconductors.^{25,26}

Theory

In the ground state, polaron formation at its simplest can be described by the Holstein Hamiltonian:^{7,27}

$$H = -t \sum_{\langle ij \rangle \sigma} (c_{i\sigma}^\dagger c_{j\sigma} + c_{j\sigma}^\dagger c_{i\sigma}) + \omega_0 \sum_i b_i^\dagger b_i + g \sum_{i,\sigma} n_{i\sigma} (b_i + b_i^\dagger) \quad (1)$$

where t is the hopping integral, $c_{i\sigma}^\dagger$ and $c_{j\sigma}$ are the creation and annihilation operators, respectively, with spin, σ , for an electron at sites i and j . U is the on-site Coulombic repulsion, n_i is the number operator for electron spin, g corresponds to the electron–phonon coupling strength, and ω_0 refers to the phonon frequency. b_i^\dagger and b_i are the creation and annihilation operators, respectively, for phonons at site i .

The Holstein Hamiltonian, while insightful regarding the balance of electron–phonon coupling strengths, phonon frequency, and hopping integral, does not sufficiently capture the physics of complex transition-metal oxides. A Hubbard U term can be added to the Holstein model to accurately describe strong on-site repulsions of the d orbitals, particularly at half-filling, as is the case for most of the Fe(III) oxides considered in this work.^{28,29} The ratio of the charge hopping integral, t , to U influences the orbital mixing within the band structure. It determines whether the material is a charge transfer insulator or a Mott insulator.³⁰ In a charge transfer insulator, the upper valence bands (VBs) are dominated by ligand orbitals, and metal d orbitals dominate the lower conduction bands (CBs). In a Mott insulator, the upper VBs and lower CBs are dominated by metal d orbitals due to the emergence of the Hubbard d band. U contributes to carrier localization and thus modulates polaron formation. A representative Hubbard–Holstein Hamiltonian can be written as:

$$H = -t \sum_{\langle ij \rangle \sigma} (c_{i\sigma}^\dagger c_{j\sigma} + c_{j\sigma}^\dagger c_{i\sigma}) + U \sum_i n_{i\uparrow} n_{i\downarrow} + \omega_0 \sum_i b_i^\dagger b_i + g \sum_{i,\sigma} n_{i\sigma} (b_i + b_i^\dagger) \quad (2)$$

This Hamiltonian can be further downfolded into a t-J–Holstein model in the limit $U \gg t$, which holds for the measured transition metal oxides in this work.^{31,32} This downfold includes the spin-exchange integral (J) and, for antiferromagnetic (AFM) materials, describes superexchange in which a spin can undergo indirect exchange mediated by a ligand between two metal sites. Superexchange is favored when metal-ligand-metal bond angles are close to 180° and scales with the bond distance and bond angles, as described by Goodenough-Kanamori rules.^{33–35} At half-filling, $J = 4t^2/U$. If $t + J \gg g$, then no polaron forms, and photoexcited carriers thermalize to the band edge. If $t + J \ll g$, a polaron forms – often without significant thermalization following photoexcitation. As J , t , and U are all interrelated, modifying one through materials design will modify the others, and thus a balance must be struck between the parameters when considering materials design that aims to tune polarons. The downfolded t-J–Holstein Hamiltonian can be written as:

$$H = -t \sum_{\langle ij \rangle \sigma} (c_{i\sigma}^\dagger c_{j\sigma} + c_{j\sigma}^\dagger c_{i\sigma}) + J \sum_{ij} \vec{S}_i \cdot \vec{S}_j + \omega_0 \sum_i b_i^\dagger b_i + g \sum_{i,\sigma} n_{i\sigma} (b_i + b_i^\dagger) \quad (3)$$

Each Hamiltonian outlined above describes different polaronic coupling regimes and models polaronic properties accordingly. The consideration of on-site repulsions and spin exchange in the Hubbard–Holstein and t-J–Holstein models, respectively, increases the complexity of each model Hamiltonian, but also acts to more accurately predict the polaronic properties of strongly electron- and spin-correlated materials.

Polaron Parameterization from Experimental Measurements

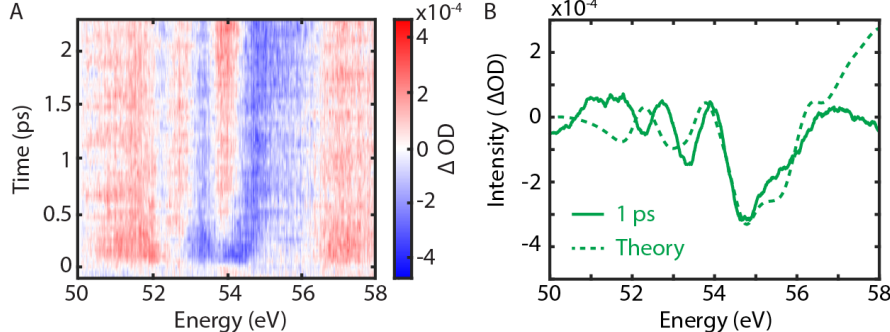


Figure 1. Representative transient XUV spectra and DFT+BSE theory. **a.** Representative transient XUV reflectivity spectra at the Fe M_{2,3} edge in GdFeO₃ centered at ~54 eV. At pump-probe overlap (t_0), a series of positive and negative peaks are observed. Immediately after photoexcitation with an 800 nm pump, an ultrafast spectral blueshift is observed around ~55 eV, which is attributed to octahedra expansion and small polaron formation. **b.** Representative experimental lineout after polaron formation is complete (1 ps) compared with DFT+BSE calculated polaronic spectra.

While these models, especially the Holstein model, have been widely applied to ground state polaronic properties, they are rarely compared to excited state polaron formation dynamics. We employ transient extreme ultraviolet (XUV) reflection-absorption spectroscopy to measure the polaron energy and phonon frequency. An example of the experimental characterization is shown in Figure 1.

In the iron oxide systems considered here, the transient XUV spectrum is dominated by the change of the angular momentum coupling and structural distortions following photoexcitation at the Fe M_{2,3} edge. This results in a blueshift of the Fe M_{2,3} edge to higher energies when photoexcited electron polaron formation occurs due to anisotropic structural distortion and carrier localization at iron sites (Figure 1A). We particularly expect electron polaron formation in charge transfer insulating iron oxides, which have conduction bands dominated by iron d orbitals; however, this may differ for intermediate and Mott insulators, which have different accessible excitation manifolds. We validate the differential spectrum of the polaron feature using a DFT+BSE calculated X-ray spectrum that accounts for photoexcited carriers

and polaronic lattice distortions (Figure 1B).^{20,36} The spectrum is then decomposed into the appropriate excited states to extract the related kinetics using singular value decomposition (Fig. 2).

As shown in Figure 2, a variety of polaron formation kinetics have been measured using transient XUV spectroscopy. In hematite, polaron formation occurs within the first electron–optical-phonon scattering time of ~ 100 fs.³⁷ In CuFeO₂, a polaron forms on the same timescale as hematite, but a *c*-axis lattice expansion on a picosecond timescale enables a delocalization of the initial polaron state.³⁸ In ErFeO₃, coherent charge hopping occurs before dephasing, and polarons are formed on a 2.3 ± 0.3 ps timescale, indicating large-polaron or mixed polaron/free electron conduction behavior.³⁹ GdFeO₃ does not form a polaron under 400 nm photoexcitation of a ligand-to-metal charge transfer (LMCT) that preserves the high-spin ground state. In contrast, 800 nm photoexcitation of a metal-to-metal charge transfer (MMCT) forms polarons in 250 ± 40 fs.²⁰ Transient XUV measurements of Fe₂SiO₄ are shown in the Supporting Information and polaron formation occurs within 130 ± 40 fs. Notably, Fe₂SiO₄ has an Fe(II) oxidation state in the ground state, while the other iron oxides measured in this work have Fe(III) oxidation states in the ground state.

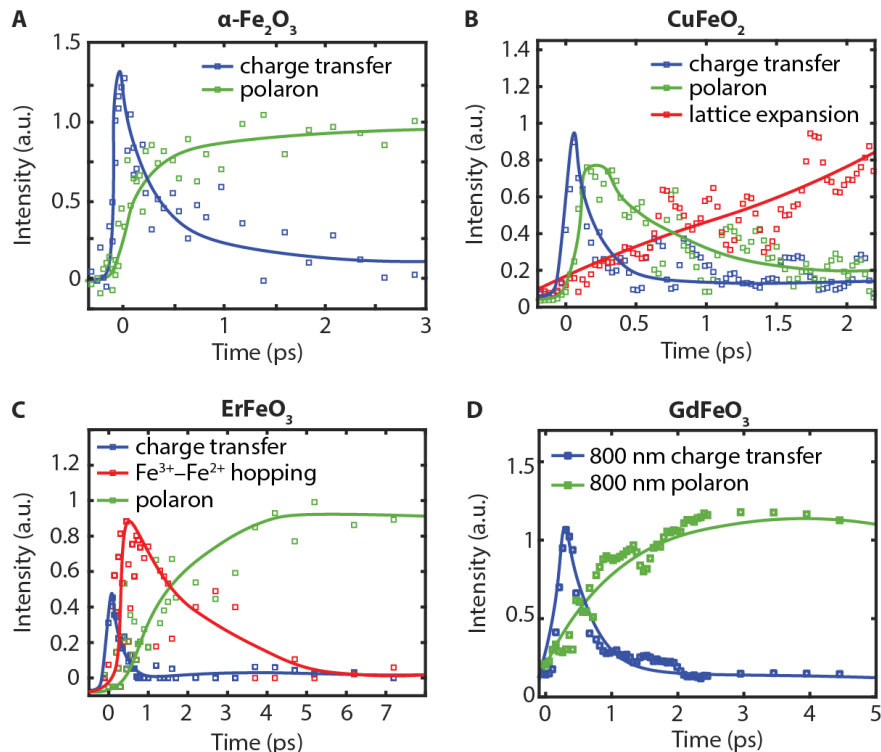


Figure 2. Formation timescales and dynamics for polaron-forming Fe-O-based materials. **a.** Hematite forms a polaron within ~ 100 fs, leaving few free carriers. **b.** CuFeO₂ forms a polaron within ~ 100 fs, which relaxes on a picosecond timescale through a *c*-axis expansion and subsequent delocalization. **c.** ErFeO₃ forms a polaron only after a period of Fe²⁺–Fe³⁺ charge hopping associated with superexchange. **d.** GdFeO₃ only forms a polaron following an 800 nm metal-to-metal charge transfer (MMCT) whereas no polarons form following a 400 nm ligand-to-metal charge transfer due to superexchange mechanisms under different spin configurations.

We have found, consistent with optical reflectivity experiments,⁴⁰ that the spectral blueshift of the XUV signal corresponding to polaron formation is approximately twice the polaron binding energy (E_{polaron}), to a first order approximation. E_{polaron} is calculated from the magnitude of the spectral shift at the Fe M_{2,3} edge, and the timescale of this shift measures the phonon energy associated with the polaron formation (ω_0). For most materials, ω_0 is on the order of the highest optical phonon frequency, which is fairly consistent for iron oxide-based materials at 80–100 meV.⁴¹ The polaron energy can be described by Equation 4:

$$E_{\text{polaron}} = -\frac{g^2}{w_0} + t \exp\left(-\frac{g^2}{\omega_0^2}\right) \cos(k) + \dots \quad (4)$$

where k is momentum. For the materials measured here, except ErFeO_3 which exhibits large-polaron-like behavior, we can truncate the sum of the polaron energy in the first term due to the small electronic bandwidths of the measured iron oxides. Using the parameterization of experimental XUV spectra and the truncation of Equation 4, we can estimate the electron–phonon coupling parameter, g . DFT+U calculations are used to approximate the electronic hopping integral t .^{42,43} Note that the expression for electronic bandwidth goes as $2dt$ where d is the dimensionality, here d is taken as three. We employ a ground-state approximation of t however we note that during photoexcitation there can be subtle changes that modify t . A Lang–Firsov approach can be used to estimate the effective electronic hopping integral (t_{eff}) following photoexcited polaron formation, however, because we approximate the electronic hopping integral (t) from ground-state theory, we consider the undressed hopping integral.^{7,44,45}

The measured and calculated parameterization of the scalar quantities of the Holstein, Hubbard–Holstein, and t-J–Holstein models for a range of polaron forming transition metal oxides are given in Table 1, following the above outlined parameterization.

Table 1. Parameters of the Holstein, Hubbard–Holstein, and t-J–Holstein Hamiltonians. All values are in units of eV. J is approximated as exchange energy per spin. – denotes no known literature value for one of the necessary parameters.

	E_{polaron}	ω_0	$2dt$	J	$g = \sqrt{\frac{E_{\text{polaron}} * \omega_0}{2dt}}$	$\lambda = \frac{g^2}{2dt\omega_0}$	$\gamma = \frac{\omega_0}{2dt}$	$g/2dt$	$4/(J/t)$
$\alpha\text{-Fe}_2\text{O}_3$	0.50 ³⁷	0.08 ⁴⁶	0.19 ³⁶	0.0097 ⁴⁷	0.20	2.63	1.26	1.05	13.07
CuFeO_2	0.35 ³⁸	0.09 ⁴⁸	0.34 ³⁸	0.017 ⁴⁹	0.18	1.03	0.79	0.52	13.26
Fe_2SiO_4	0.23	0.10 ⁵⁰	0.56 ⁵¹	0.0046 ⁵²	0.15	0.40	0.55	0.27	81.16
ErFeO_3	0.05 ³⁹	0.02 ³⁹	0.91 ³⁹	0.38 ⁵³	0.03	0.05	0.07	0.03	1.59
BiFeO_3	0.65 ⁵⁴	0.07 ^{54–56}	0.33 ⁵⁴	0.16 ⁵⁷	0.21	1.97	0.64	0.65	1.34
$\alpha\text{-FeOOH}$	0.55 ⁵⁸	0.08 ^{58–60}	0.22 ⁶¹	0.19 ⁶²	0.21	2.50	1.09	0.84	0.88
GdFeO_3	0.20 ²⁰	0.07 ⁴¹	0.13 ²⁰	0.16 ⁶³	0.12	1.54	1.62	0.91	0.55
a-TiO_2	0.10 ⁶⁴	0.11 ^{65,66}	1.51 ⁶⁷	–	0.10	0.07	0.21	0.07	–
BiVO_4	0.44 ⁶⁸	0.10 ⁶⁹	0.79 ⁷⁰	–	0.21	1.86	0.39	0.27	–

For some of the systems described in Table 1, it is important to consider superexchange and the Hubbard interaction. Of the above materials, GdFeO_3 and Fe_2SiO_4 are the only materials that are not charge transfer insulators. A charge transfer insulator has a valence band (VB) dominated by O 2p orbitals and a conduction band (CB) primarily composed of Fe 3d orbitals. GdFeO_3 is an intermediate insulator, meaning that the VB is composed of mixed Fe and O orbital character, the CB is dominated by Fe d orbitals much like charge transfer insulators. This enables above band gap excitation of both LCMT and MMCT transitions. On the other hand, Fe_2SiO_4 is a Mott-insulator, meaning the Fe 3d orbitals dominate both the VB and CB, enabling primarily MMCT transitions. Superexchange at half-filling goes as $J = 4t^2/U$, so changes to either J or U will modulate polaron formation. We also include Fe_2SiO_4 as an Fe(II) system to visualize how well the model captures polaronic properties above half-filling. To approximate the superexchange process, J is taken as the exchange energy per spin, which is equivalent to zJ_1S^2 where z is the connectivity, J_1 corresponds to values derived from inelastic neutron scattering experiments in literature, and S corresponds to the spin of the system.^{71,72}

Mapping to Phase Diagrams

Here we consider the experimentally derived parameters in terms of the phase diagrams of the Holstein, Hubbard–Holstein, and t-J–Holstein Hamiltonians. These phase diagrams serve to visualize the influence

of different parameters on properties such as polaron strength, carrier localization, on-site repulsions, and spin exchange. We map the measured iron oxide materials to identify different material properties that modulate polaronic parameters, thereby informing design rules.

For the Holstein phase diagram, we use two scalar ratios. The first relates to the polaron's strength, $g^2/2dt\omega_0$. The second is $\omega_0/2dt$, which describes the mobility of the polaron via phonons versus free-carrier conduction. Based on Table 1 and the scalar ratios, we construct a phase diagram mapping the measured and derived parameters within the stated approximations in Figure 3. We consider the atomic limit to be the upper right corner of Figure 3, where carriers are completely localized. In the bottom left of Figure 3, photoexcited carriers approach a free carrier limit. We can make a general yet representative cutoff between large and small polarons based on when Equation 4 approaches zero. This is a blurred, approximate transition that is widely debated in the literature, but it is depicted here for simplicity.^{6,73,74}

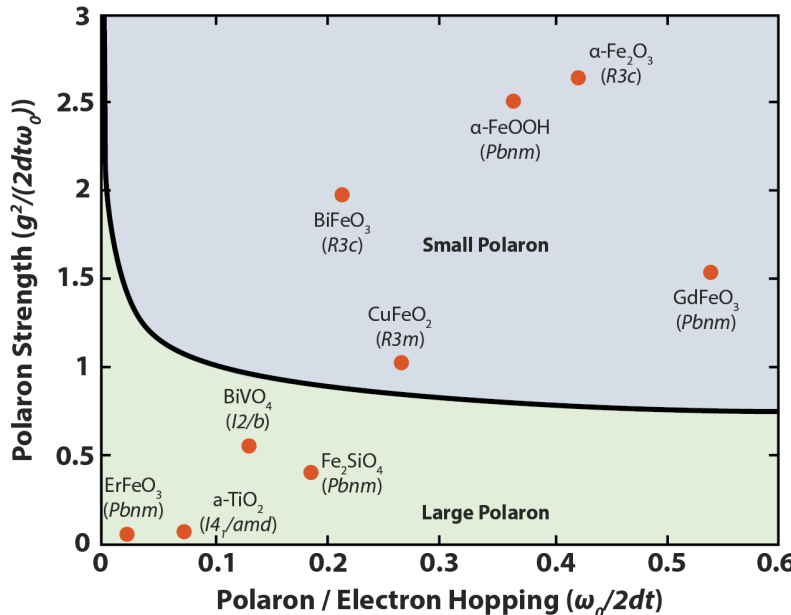


Figure 3. Mapping measured polarons onto a Holstein Hamiltonian's phase diagram. Materials and their symmetry group are shown next to the orange dots. The transition between small (blue) and large (green) polarons is schematically denoted by color shading and the solid black line. The upper right corner that we attribute to the atomic limit where carriers are strongly localized depicts a regime where $t \ll g$, while the lower left corner denotes a free conduction regime in which $t \gg g$.

The circles in Figure 3 represent transient XUV data from References^{20,37–39,54,58,75}, XUV spectra for Fe₂SiO₄ in the Supporting Information, and optical transient absorption spectra for BiVO₄.⁶⁸ The agreement between measured polaron properties, where the material falls on the phase diagram with respect to the scaling factors, and the small-to-large polaron crossover is found to be qualitatively predictive. For example, α-Fe₂O₃ and α-FeOOH are found to be in the upper right corner near the limit of strong polarons and low mobility, which has been widely experimentally demonstrated.^{76–78} CuFeO₂, which has been found to have a polaron with a weaker binding energy than hematite and goethite due to a coherent c-axis lattice expansion that delocalizes the polaron, falls into the middle part of the diagram. BiVO₄, which is often debated as having an intermediate-sized polaron, falls on the left boundary close to the crossover between small and large polarons.^{79,80} ErFeO₃ can be found in the lower left corner because $t \gg g$ due to strong superexchange interactions, which result in a strong electron hopping integral (t) and weakened electron–phonon coupling strength (g).⁸¹ Anatase TiO₂ a large polaron material, is also shown for comparison. It is notable that the Holstein model does not well describe materials in the free-carrier limit as $E_{polaron} \sim 2dt$.^{7,12}

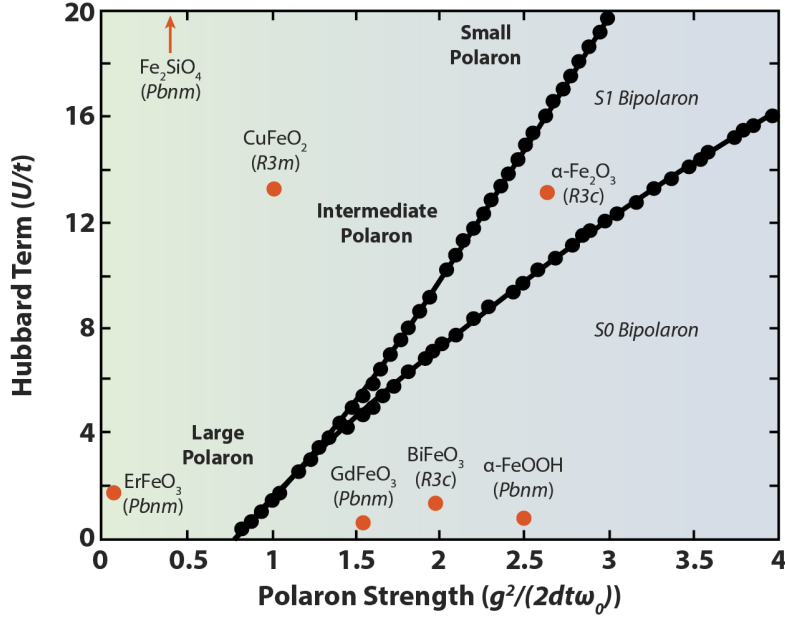


Figure 4. Mapping measured polarons to the phase diagram of the Hubbard–Holstein Hamiltonian. Small (blue) to large (green) polaron behavior is depicted by the color shading. The black dotted line depicts the boundary between individual polarons and bipolarons. Orange dots depict each measured iron oxide. We do not include the measured materials for which there are no reported J values. Adapted from reference ⁸².

We next increase the complexity of our phase diagram by considering the Hubbard–Holstein model in Figure 4. Only materials with a reported J value, as given in Table 1, are shown. We do not consider literature reported U values as they vary widely depending on the level of theory applied. The Hubbard parameter acts in multiple regimes. On the phase diagram, it is plotted on the left-hand side by using the relation $J = 4t^2/U$ where J is the exchange energy per spin. We note that this is only a first-order approximation, since the relation between U and J depend on many-body wave functions. On the x-axis the polaron strength is parameterized the same as the Holstein model. Depending on the ratio of U to the polaron strength, the Hubbard–Holstein model predicts a range of large to small polaron in both extended and bipolaron states. For a relatively small electron–phonon coupling strength, the polarons exist independently of each other. Under strong electron–phonon coupling, the U term is overcome, and the bipolaron can either exist on the same site (S0) or neighboring bound sites (S1).

In the weak-coupling region, where U dominates the electron–phonon coupling strength, we find that the model accurately maps the small-to-intermediate-to-large polaron regime for the single-polaron case, providing more detail than the Holstein model alone. Over localization of the Hubbard–Holstein model is a known issue, although multiple predictions do exist for bipolarons – the literature remains sparse in their measurement for these systems.^{83–85} However, including the Hubbard term for these transition-metal oxides yields a more accurate delineation of single-polaron species and their classification.

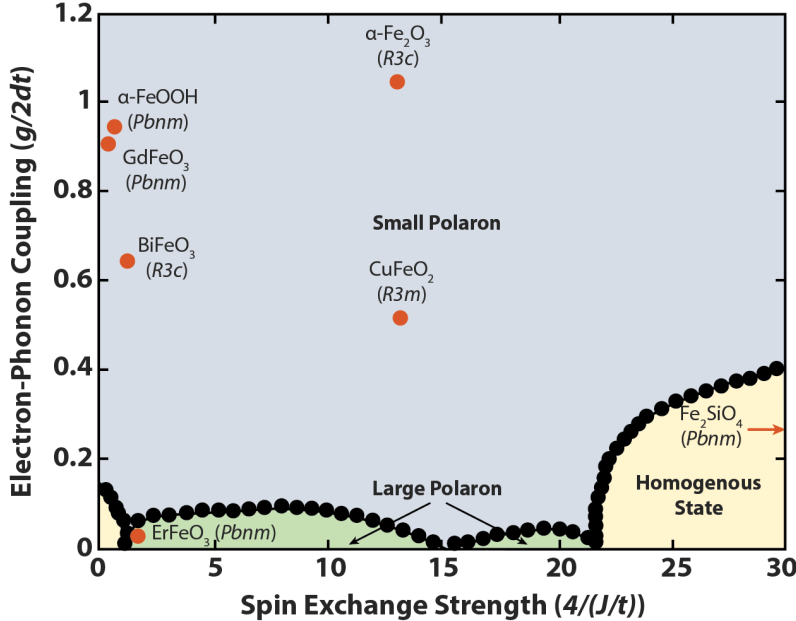


Figure 5. Experimentally derived polaronic parameters mapped to a phase diagram of the t-J–Holstein model. Regions corresponding to small polaron (blue), large polaron (green), and near-free carrier (yellow – homogenous state) behavior are shown by shading. Materials are represented by an orange dot and labelled to include their symmetry group. Adapted from reference ⁸⁶.

We then map the measured iron oxides onto the phase diagram of the t-J–Holstein Hamiltonian for the materials where measured J values exist in literature (Table 1). Figure 5 shows the phase diagram for the ratios of $g/2dt$ and $4/(J/t)$. The parameters g and J must be scaled by that material's t for comparison to the phase diagram of Reference ⁸⁶. Figure 5 compares how polaron formation varies as J is modulated for the measured materials. Areas corresponding to small polaron, large polaron, and near-free carrier conduction (homogenous state) are mapped. The materials that form small polarons mostly agree with the small polaron designation on the phase diagram, while ErFeO_3 , with its balance of charge hopping and spin exchange, falls into the large polaron regime of the phase diagram. The diagram indicates that tuning the spin exchange interaction is an effective, though not necessarily straightforward, way to control the small polaron. It must be balanced against the strength of the electron–phonon coupling parameter. Considering these two parameters together reveals that tuning the spin exchange can lead to a rich range of polaron sizes, dynamics, and strengths, extending beyond the electron–phonon parameter of the Holstein model. Superexchange depends on both the Fe–O bond length and the Fe–O–Fe bond angle, as well as spin interactions, providing general guidelines for polaron-based material design.

Conclusions

We find that the Holstein, Hubbard–Holstein, and t-J–Holstein models can be used to describe excited state polaronic dynamics across a range of transition metal oxides. We find that experimental transient XUV experiments can be parameterized within each Hamiltonian's framework and applied to phase-space diagrams previously limited to theory, yielding good agreement between experiment and theory. In particular, the t-J–Holstein Hamiltonian is particularly descriptive and yields the clearest set of design parameters by incorporating spin degrees of freedom. Although this is of particular interest for iron oxides with half-filled d orbitals, the design parameter can be generalized to other transition-metal oxides for which measured superexchange interactions are available.^{87,88} We demonstrate that tuning electron–phonon coupling strength (g), electron localization (t), and spin exchange (J) can be leveraged to suppress or control polaron formation in transition metal oxides. Because these values are interrelated, one must balance them to optimize control over polarons. This work combines experimental data with ground-state theoretical models to provide robust phase diagrams that inform polaron design and extract specific material parameters that can be tuned for polaron modulation.

Acknowledgements

This material is based on work performed by the Liquid Sunlight Alliance, which is supported by the U.S. Department of Energy, Office of Science, Office of Basic Energy Sciences, Fuels from Sunlight Hub under Award Number DE-SC0021266. This research used resources of the National Energy Research Scientific Computing Center, a DOE Office of Science User Facility supported by the Office of Science of the U.S. Department of Energy under contract no. DE-AC02-05CH11231 using NERSC award BES-ERCAP0024109. The computations presented here were, in part, conducted in the Resnick High Performance Computing Center, a facility supported by the Resnick Sustainability Institute at the California Institute of Technology. J.L.M. acknowledges support by the National Science Foundation Graduate Research Fellowship Program under Grant No. 1745301. Any opinions, findings, and conclusions or recommendations expressed in this material are those of the author(s) and do not necessarily reflect the views of the National Science Foundation.

References

- (1) Cheng, C.; Zhou, Z.; Long, R. Time-Domain View of Polaron Dynamics in Metal Oxide Photocatalysts. *J. Phys. Chem. Lett.* **2023**, *14* (49), 10988–10998. <https://doi.org/10.1021/acs.jpclett.3c02869>.
- (2) Yang, K.; Kwon, D.; Nam, S.; Kim, J.; Chung, Y. S.; Yoo, H.; Park, I.; Park, Y.; Kim, J. W.; Lee, J. Interfacial Exciton-Polaron Quenching in Organic Light-Emitting Diodes. *Phys. Rev. X* **2024**, *14* (4), 041009. <https://doi.org/10.1103/PhysRevX.14.041009>.
- (3) Ghosh, R.; Spano, F. C. Excitons and Polarons in Organic Materials. *Acc. Chem. Res.* **2020**, *53* (10), 2201–2211. <https://doi.org/10.1021/acs.accounts.0c00349>.
- (4) Liu, X.; Gao, K.; Li, Y.; Fu, J.; Wei, J.; Xie, S. Polaron Formation Dynamics in Conducting Polymers. *Synth. Met.* **2007**, *157* (8), 380–385. <https://doi.org/10.1016/j.synthmet.2007.04.008>.
- (5) Naamneh, M.; O’Quinn, E. C.; Paris, E.; McNally, D.; Tseng, Y.; Pudełko, W. R.; Gawryluk, D. J.; Shamblin, J.; Cohen-Stead, B.; Shi, M.; Radovic, M.; Lang, M. K.; Schmitt, T.; Johnston, S.; Plumb, N. C. Persistence of Small Polarons into the Superconducting Doping Range of $\text{Ba}_{1-x}\text{K}_x\text{BiO}_3$. *Phys. Rev. Research* **2025**, *7* (4), 043082. <https://doi.org/10.1103/s3p1-cy1s>.
- (6) Franchini, C.; Reticcioli, M.; Setvin, M.; Diebold, U. Polarons in Materials. *Nat. Rev. Mater.* **2021**, *6* (7), 560–586. <https://doi.org/10.1038/s41578-021-00289-w>.
- (7) *Polarons in Advanced Materials*; Alexandrov, A. S., Ed.; Hull, R., Osgood, R. M., Parisi, J., Warlimont, H., Series Eds.; Springer Series in Materials Science; Springer Netherlands: Dordrecht, 2007; Vol. 103. <https://doi.org/10.1007/978-1-4020-6348-0>.
- (8) Yim, C.-M.; Allan, M.; Pang, C. L.; Thornton, G. Scanning Tunneling Microscopy Visualization of Polaron Charge Trapping by Hydroxyls on $\text{TiO}_2(110)$. *J. Phys. Chem. C* **2024**, *128* (33), 14100–14106. <https://doi.org/10.1021/acs.jpcc.4c03751>.
- (9) Fehske, H.; Trugman, S. A. Numerical Solution of the Holstein Polaron Problem. *Polarons in Advanced Materials*; Alexandrov, A. S., Ed.; Springer Netherlands: Dordrecht, 2007; pp 393–461. https://doi.org/10.1007/978-1-4020-6348-0_10.
- (10) Johnston, C. R.; Speelman, R.; Arcidiacono, A.; Bridgewater, C.; Rassouli, L.; Ma, X.; Vargas-Hurlston, I.; Kupferberg, J.; Martin, L.; Martinson, A. B. F.; Dupuis, M.; Geiger, F. M.; King, S. B. Watching Polarons Dance: Coherent Carrier–Phonon Coupling in Hematite Revealed by Transient Absorption Spectroscopy. *J. Am. Chem. Soc.* **2025**, *147* (44), 40338–40346. <https://doi.org/10.1021/jacs.5c11324>.
- (11) Bhattacharyya, S.; Sayer, T.; Montoya-Castillo, A. Nonequilibrium Relaxation Exponentially Delays the Onset of Quantum Diffusion. *Proc. Natl. Acad. Sci.* **2025**, *122* (19), e2424582122. <https://doi.org/10.1073/pnas.2424582122>.
- (12) Kloss, B.; Reichman, D. R.; Tempelaar, R. Multiset Matrix Product State Calculations Reveal Mobile Franck-Condon Excitations Under Strong Holstein-Type Coupling. *Phys. Rev. Lett.* **2019**, *123* (12), 126601. <https://doi.org/10.1103/PhysRevLett.123.126601>.
- (13) Emin, D. Transport Properties of Small Polarons. *J. Solid State Chem.* **1975**, *12* (3), 246–252. [https://doi.org/10.1016/0022-4596\(75\)90314-X](https://doi.org/10.1016/0022-4596(75)90314-X).
- (14) Fratini, S.; Ciuchi, S. Dynamical Mean-Field Theory of Transport of Small Polarons. *Phys. Rev. Lett.* **2003**, *91*

- (25), 256403. <https://doi.org/10.1103/PhysRevLett.91.256403>.
- (15) Holstein, T. Studies of Polaron Motion: Part II. The “Small” Polaron. *Ann. Phys.* **2000**, *281* (1), 725–773. <https://doi.org/10.1006/aphy.2000.6021>.
- (16) Zhao, G.; Smolyaninova, V.; Prellier, W.; Keller, H. Electrical Transport in the Ferromagnetic State of Manganites: Small-Polaron Metallic Conduction at Low Temperatures. *Phys. Rev. Lett.* **2000**, *84* (26), 6086–6089. <https://doi.org/10.1103/PhysRevLett.84.6086>.
- (17) Carneiro, L. M.; Cushing, S. K.; Liu, C.; Su, Y.; Yang, P.; Alivisatos, A. P.; Leone, S. R. Excitation-Wavelength-Dependent Small Polaron Trapping of Photoexcited Carriers in α -Fe₂O₃. *Nat. Mater.* **2017**, *16* (8), 819–825. <https://doi.org/10.1038/nmat4936>.
- (18) Biswas, S.; Wallentine, S.; Bandaranayake, S.; Baker, L. R. Controlling Polaron Formation at Hematite Surfaces by Molecular Functionalization Probed by XUV Reflection-Absorption Spectroscopy. *J. Chem. Phys.* **2019**, *151* (10), 104701. <https://doi.org/10.1063/1.5115163>.
- (19) Gao, C.; Zhang, L.; Zheng, Q.; Zhao, J. Tuning the Lifetime of Photoexcited Small Polarons on Rutile TiO₂ Surface via Molecular Adsorption. *J. Phys. Chem. C* **2021**, *125* (49), 27275–27282. <https://doi.org/10.1021/acs.jpcc.1c07697>.
- (20) Mendes, J. L.; Shin, H. J.; Seo, J. Y.; Lee, N.; Choi, Y. J.; Varley, J. B.; Cushing, S. K. Dynamic Competition between Hubbard and Superexchange Interactions Selectively Localizes Electrons and Holes through Polarons. *J. Am. Chem. Soc.* **2025**, *141* (19), 16018–16026. <https://doi.org/10.1021/jacs.4c16837>.
- (21) Batzill, M. Fundamental Aspects of Surface Engineering of Transition Metal Oxide Photocatalysts. *Energy Environ. Sci.* **2011**, *4* (9), 3275–3286. <https://doi.org/10.1039/C1EE01577J>.
- (22) Emin, D. Formation and Hopping Motion of Molecular Polarons. *Phys. Rev. B* **2000**, *61* (21), 14543–14553. <https://doi.org/10.1103/PhysRevB.61.14543>.
- (23) Rettie, A. J. E.; Chemelewski, W. D.; Emin, D.; Mullins, C. B. Unravelling Small-Polaron Transport in Metal Oxide Photoelectrodes. *J. Phys. Chem. Lett.* **2016**, *7* (3), 471–479. <https://doi.org/10.1021/acs.jpclett.5b02143>.
- (24) Liu, X.; Gao, K.; Li, Y.; Fu, J.; Wei, J.; Xie, S. Polaron Formation Dynamics in Conducting Polymers. *Synth. Met.* **2007**, *157* (8), 380–385. <https://doi.org/10.1016/j.synthmet.2007.04.008>.
- (25) Kudinov, E. K. Model of a Polaron Superconductor. *Phys. Solid State* **2002**, *44* (4), 692–703. <https://doi.org/10.1134/1.1470561>.
- (26) Mott, N. F. Polaron Models of High-Temperature Superconductors. *J. Phys. Condens. Matter* **1993**, *5* (22), 3487. <https://doi.org/10.1088/0953-8984/5/22/003>.
- (27) Holstein, T. Studies of Polaron Motion: Part I. The Molecular-Crystal Model. *Ann. Phys.* **1959**, *8* (3), 325–342. [https://doi.org/10.1016/0003-4916\(59\)90002-8](https://doi.org/10.1016/0003-4916(59)90002-8).
- (28) Berger, E.; Valášek, P.; Von Der Linden, W. Two-Dimensional Hubbard-Holstein Model. *Phys. Rev. B* **1995**, *52* (7), 4806–4814. <https://doi.org/10.1103/PhysRevB.52.4806>.
- (29) Chatterjee, J.; Das, A. N. Role of the Superexchange Interaction in Magnetic Transition and Polaron Crossover. *Phys. B Condens. Matter* **2004**, *348* (1), 89–94. <https://doi.org/10.1016/j.physb.2003.11.075>.
- (30) Bu, X.; Li, Y. Optical Signature for Distinguishing between Mott-Hubbard, Intermediate, and Charge-Transfer Insulators. *Phys. Rev. B* **2022**, *106* (24), L241101. <https://doi.org/10.1103/PhysRevB.106.L241101>.
- (31) Dobry, A.; Greco, A.; Koval, S.; Riera, J. Exact Diagonalization Study of the Two-Dimensional t-J-Holstein Model. *Phys. Rev. B* **1995**, *52* (19), 13722–13725. <https://doi.org/10.1103/PhysRevB.52.13722>.
- (32) Vidmar, L.; Bonča, J.; Maekawa, S. Optical Conductivity in the t-J Holstein Model. *Phys. Rev. B* **2009**, *79* (12), 125120. <https://doi.org/10.1103/PhysRevB.79.125120>.
- (33) Whangbo, M.-H.; Koo, H.-J.; Dai, D.; Jung, D. Effect of Metal–Ligand Bond Lengths on Superexchange Interactions in Jahn–Teller d⁴ Ion Systems: Spin Dimer Analysis of the Magnetic Structure of Marokite CaMn₂O₄. *Inorg. Chem.* **2002**, *41* (21), 5575–5581. <https://doi.org/10.1021/ic0202458>.
- (34) Feinberg, D.; Germain, P.; Grilli, M.; Seibold, G. Joint Superexchange–Jahn-Teller Mechanism for Layered Antiferromagnetism in LaMnO₃. *Phys. Rev. B* **1998**, *57* (10), R5583–R5586. <https://doi.org/10.1103/PhysRevB.57.R5583>.
- (35) Takada, Y.; Masaki, M. Polarons in Jahn–Teller Crystals: Intrinsic Difference between E_g and t_{2g} Electrons. *J. Supercond. Nov. Magn.* **2007**, *20* (7), 629–633. <https://doi.org/10.1007/s10948-007-0280-1>.

- (36) Klein, I. M.; Liu, H.; Nimlos, D.; Krotz, A.; Cushing, S. K. Ab Initio Prediction of Excited-State and Polaron Effects in Transient XUV Measurements of α -Fe₂O₃. *J. Am. Chem. Soc.* **2022**, *144* (28), 12834–12841. <https://doi.org/10.1021/jacs.2c03994>.
- (37) Carneiro, L. M.; Cushing, S. K.; Liu, C.; Su, Y.; Yang, P.; Alivisatos, A. P.; Leone, S. R. Excitation-Wavelength-Dependent Small Polaron Trapping of Photoexcited Carriers in α -Fe₂O₃. *Nat. Mater.* **2017**, *16* (8), 819–825. <https://doi.org/10.1038/nmat4936>.
- (38) Mendes, J. L.; Bhattacharyya, S.; Huang, C.; Michelsen, J. M.; Klein, I. M.; Babbe, F.; Sayer, T.; Li, T.; Cooper, J. K.; Liu, H.; Ginsberg, N. S.; Montoya-Castillo, A.; Cushing, S. K. Coherent and Dynamic Small Polaron Delocalization in CuFeO₂. arXiv **2025**. <https://doi.org/10.48550/ARXIV.2510.16222>.
- (39) Kim, Y.-J.; Mendes, J. L.; Michelsen, J. M.; Shin, H. J.; Lee, N.; Choi, Y. J.; Cushing, S. K. Coherent Charge Hopping Suppresses Photoexcited Small Polarons in ErFeO₃ by Antiadiabatic Formation Mechanism. *Sci. Adv.* **2024**, *10* (12), eadk4282. <https://doi.org/10.1126/sciadv.adk4282>.
- (40) Ahmad, J.; Uwe, H. Small-Polaron Excitations in Ba_{1-x}K_xBiO₃ Studied by Optical Reflectivity Measurements. *Phys. Rev. B* **2005**, *72* (12), 125103. <https://doi.org/10.1103/PhysRevB.72.125103>.
- (41) Panneerselvam, I. R.; Baldo, C.; Sahasranaman, M.; Murugesan, S.; Rangaswamy, N.; Pai, S. D. K. R.; Selvarathinam, Y. Large Power Factors in Wide Band Gap Semiconducting RFeO₃ Materials for High-Temperature Thermoelectric Applications. *ACS Appl. Energy Mater.* **2020**, *3*, 11, 11193–11205. <https://doi.org/10.1021/acsaem.0c02128>
- (42) Chandler, C. J.; Prosko, C.; Marsiglio, F. The Effect of Next-Nearest Neighbour Hopping in the One, Two, and Three Dimensional Holstein Model. *Sci. Rep.* **2016**, *6* (1), 32591. <https://doi.org/10.1038/srep32591>.
- (43) Souza, T. X. R.; Marsiglio, F. Systematic Study of the Superconducting Critical Temperature in Two- and Three-Dimensional Tight-Binding Models: A Possible Scenario for Superconducting H₃S. *Phys. Rev. B* **2016**, *94* (18), 184509. <https://doi.org/10.1103/PhysRevB.94.184509>.
- (44) Stephan, W.; Capone, M.; Grilli, M.; Castellani, C. Influence of Electron-Phonon Interaction on Superexchange. *Phys. Lett. A* **1997**, *227* (1-2), 120–126. [https://doi.org/10.1016/S0375-9601\(96\)00950-4](https://doi.org/10.1016/S0375-9601(96)00950-4).
- (45) Hohenadler, M.; von der Linden, W. Lang-Firsov Approaches to Polaron Physics: From Variational Methods to Unbiased Quantum Monte Carlo Simulations. In *Polarons in Advanced Materials*; Alexandrov, A. S., Ed.; Springer Netherlands: Dordrecht, 2007; pp 463–502. https://doi.org/10.1007/978-1-4020-6348-0_11.
- (46) Shelton, J. L.; Knowles, K. E. Polaronic Optical Transitions in Hematite (α -Fe₂O₃) Revealed by First-Principles Electron–Phonon Coupling. *J. Chem. Phys.* **2022**, *157* (17), 174703. <https://doi.org/10.1063/5.0116233>.
- (47) Hill, A. H.; Jacobsen, H.; Stewart, J. R.; Jiao, F.; Jensen, N. P.; Holm, S. L.; Mutka, H.; Seydel, T.; Harrison, A.; Lefmann, K. Magnetic Properties of Nano-Scale Hematite, α -Fe₂O₃, Studied by Time-of-Flight Inelastic Neutron Spectroscopy. *J. Chem. Phys.* **2014**, *140* (4), 044709. <https://doi.org/10.1063/1.4862235>.
- (48) Klobes, B.; Herlitschke, M.; Rushchanskii, K. Z.; Wille, H.-C.; Lummen, T. T. A.; Van Loosdrecht, P. H. M.; Nugroho, A. A.; Hermann, R. P. Anisotropic Lattice Dynamics and Intermediate-Phase Magnetism in Delafossite CuFeO₂. *Phys. Rev. B* **2015**, *92* (1), 014304. <https://doi.org/10.1103/PhysRevB.92.014304>.
- (49) Ye, F.; Fernandez-Baca, J. A.; Fishman, R. S.; Ren, Y.; Kang, H. J.; Qiu, Y.; Kimura, T. Magnetic Interactions in the Geometrically Frustrated Triangular Lattice Antiferromagnet CuFeO₂. *Phys. Rev. Lett.* **2007**, *99* (15), 157201. <https://doi.org/10.1103/PhysRevLett.99.157201>.
- (50) Ghose, S.; Hastings, J. M.; Choudhury, N.; Chaplot, S. L.; Rao, K. R. Phonon Dispersion Relation in Fayalite, Fe₂SiO₄. *Phys. B Condens. Matter* **1991**, *174* (1), 83–86. [https://doi.org/10.1016/0921-4526\(91\)90582-Y](https://doi.org/10.1016/0921-4526(91)90582-Y).
- (51) Jiang, X.; Guo, G. Y. Electronic Structure, Magnetism, and Optical Properties of Fe₂SiO₄ Fayalite at Ambient and High Pressures: A GGA + U Study. *Phys. Rev. B* **2004**, *69* (15), 155108. <https://doi.org/10.1103/PhysRevB.69.155108>.
- (52) Schmidt, W.; Brotzeller, C.; Geick, R.; Schweiss, P.; Treutmann, W. Magnon-Phonon Coupling in Fe₂SiO₄. *J. Magn. Magn. Mater.* **1992**, *104–107*, 1049–1050. [https://doi.org/10.1016/0304-8853\(92\)90484-6](https://doi.org/10.1016/0304-8853(92)90484-6).
- (53) Koshizuka, N.; Ushioda, S. Inelastic-Light-Scattering Study of Magnon Softening in ErFeO₃. *Phys. Rev. B* **1980**, *22* (11), 5394–5399. <https://doi.org/10.1103/PhysRevB.22.5394>.
- (54) Chen, W.; Wang, T.; Yu, C.-C.; Jing, Y.; Li, X.; Xiong, W. Small Polaron-Induced Ultrafast Ferroelectric Restoration in BiFeO₃. *Phys. Rev. X* **2025**, *15* (2), 021046. <https://doi.org/10.1103/PhysRevX.15.021046>.
- (55) Fukumura, H.; Matsui, S.; Harima, H.; Takahashi, T.; Itoh, T.; Kisoda, K.; Tamada, M.; Noguchi, Y.; Miyayama, M. Observation of Phonons in Multiferroic BiFeO₃ Single Crystals by Raman Scattering. *J. Phys.: Condens. Matter*

- 2007**, *19*, 365224. . <https://doi.org/10.1088/0953-8984/19/36/365224>.
- (56) Wang, Y.; Saal, J. E.; Wu, P.; Wang, J.; Shang, S.; Liu, Z.-K.; Chen, L.-Q. First-Principles Lattice Dynamics and Heat Capacity of BiFeO₃. *Acta Mater.* **2011**, *59* (10), 4229–4234. <https://doi.org/10.1016/j.actamat.2011.03.047>.
- (57) Jeong, J.; Goremychkin, E. A.; Guidi, T.; Nakajima, K.; Jeon, G. S.; Kim, S.-A.; Furukawa, S.; Kim, Y. B.; Lee, S.; Kiryukhin, V.; Cheong, S.-W.; Park, J.-G. Spin Wave Measurements over the Full Brillouin Zone of Multiferroic BiFeO₃. *Phys. Rev. Lett.* **2012**, *108* (7), 077202. <https://doi.org/10.1103/PhysRevLett.108.077202>.
- (58) Molesky, I. J. P.; Cushing, S. K.; Carneiro, L. M.; Lee, A.; Ondry, J. C.; Dahl, J. C.; Chang, H.-T.; Alivisatos, A. P.; Leone, S. R. Photoexcited Small Polaron Formation in Goethite (α -FeOOH) Nanorods Probed by Transient Extreme Ultraviolet Spectroscopy. *J. Phys. Chem. Lett.* **2018**, *9* (14), 4120–4124. <https://doi.org/10.1021/acs.jpclett.8b01525>.
- (59) Hu, Q.; Kim, D. Y.; Yang, W.; Yang, L.; Meng, Y.; Zhang, L.; Mao, H.-K. FeO₂ and FeOOH under Deep Lower-Mantle Conditions and Earth's Oxygen–Hydrogen Cycles. *Nature* **2016**, *534* (7606), 241–244. <https://doi.org/10.1038/nature18018>.
- (60) Khan, I.; Hashmi, A.; Farooq, M. U.; Hong, J. Two-Dimensional Magnetic Semiconductor in Feroxyhyte. *ACS Appl. Mater. Interfaces* **2017**, *9* (40), 35368–35375. <https://doi.org/10.1021/acsami.7b08499>.
- (61) Liu, X.; Liu, H.; Zong, M.; Chen, M.; He, H.; Wang, R.; Lu, X. Mn Substitution and Distribution in Goethite and Influences on Its Photocatalytic Properties: A Combined Study Using First-Principles Calculations and Photocatalytic Experiments. *Am. Mineral.* **2023**, *108* (5), 968–977. <https://doi.org/10.2138/am-2022-8182>.
- (62) Abrashev, M. V.; Ivanov, V. G.; Stefanov, B. S.; Todorov, N. D.; Rosell, J.; Skumryev, V. Raman Spectroscopy of alpha-FeOOH (goethite) Near Antiferromagnetic to Paramagnetic Phase Transition. *J. Appl. Phys.* **2020**, *127* (20): 205108. <https://doi.org/10.1063/5.0006352>.
- (63) Zhu, X.-H.; Xiao, X.-B.; Chen, X.-R.; Liu, B.-G. Electronic Structure, Magnetism and Optical Properties of Orthorhombic GdFeO₃ from First Principles. *RSC Adv.* **2017**, *7* (7), 4054–4061. <https://doi.org/10.1039/C6RA25259A>.
- (64) De Lile, J. R.; Kang, S. G.; Son, Y.-A.; Lee, S. G. Investigating Polaron Formation in Anatase and Brookite TiO₂ by Density Functional Theory with Hybrid-Functional and DFT + U Methods. *ACS Omega* **2019**, *4*, 5, 8056–8064. <https://doi.org/10.1021/acsomega.9b00443>.
- (65) Kang, Y.; Peelaers, H.; Van de Walle, C. G. First-Principles Study of Electron-Phonon Interactions and Transport in Anatase TiO₂. *Phys. Rev. B* **2019**, *100* (12), 121113. <https://doi.org/10.1103/PhysRevB.100.121113>.
- (66) Moser, S.; Moreschini, L.; Jaćimović, J.; Barišić, O. S.; Berger, H.; Magrez, A.; Chang, Y. J.; Kim, K. S.; Bostwick, A.; Rotenberg, E.; Forró, L.; Grioni, M. Tunable Polaronic Conduction in Anatase TiO₂. *Phys. Rev. Lett.* **2013**, *110* (19), 196403. <https://doi.org/10.1103/PhysRevLett.110.196403>.
- (67) Labat, F.; Baranek, P.; Adamo, C. Structural and Electronic Properties of Selected Rutile and Anatase TiO₂ Surfaces: An Ab Initio Investigation. *J. Chem. Theory Comput.* **2008**, *4* (2), 341–352. <https://doi.org/10.1021/ct700221w>.
- (68) Zhang, J.; Shi, J.; Chen, Y.; Zhang, K. H. L.; Yang, Y. Bimolecular Self-Trapped Exciton Formation in Bismuth Vanadate. *J. Phys. Chem. Lett.* **2022**, *13* (42), 9815–9821. <https://doi.org/10.1021/acs.jpclett.2c02596>.
- (69) Liu, T.; Zhang, X.; Guan, J.; Catlow, C. R. A.; Walsh, A.; Sokol, A. A.; Buckeridge, J. Insight into the Fergusonite–Scheelite Phase Transition of ABO₄-Type Oxides by Density Functional Theory: A Case Study of the Subtleties of the Ground State of BiVO₄. *Chem. Mater.* **2022**, *34* (12), 5334–5343. <https://doi.org/10.1021/acs.chemmater.1c04417>.
- (70) Yin, W.-J.; Wei, S.-H.; Al-Jassim, M. M.; Turner, J.; Yan, Y. Doping Properties of Monoclinic BiVO₄ Studied by First-Principles Density-Functional Theory. *Phys. Rev. B* **2011**, *83* (15), 155102. <https://doi.org/10.1103/PhysRevB.83.155102>.
- (71) Radcliffe, J. M. Approximate Free Energies for Heisenberg Ferromagnets. *Phys. Rev.* **1968**, *165* (2), 635–641. <https://doi.org/10.1103/PhysRev.165.635>.
- (72) Anderson, P. W. Antiferromagnetism. Theory of Superexchange Interaction. *Phys. Rev.* **1950**, *79* (2), 350–356. <https://doi.org/10.1103/PhysRev.79.350>.
- (73) Zhang, C. Light Polarons with Electron-Phonon Coupling. *Phys. Rev. B* **2024**, *109* (16), 165119. <https://doi.org/10.1103/PhysRevB.109.165119>.
- (74) Zhang, K.; Fu, C.; Kelly, S.; Liang, L.; Kang, S.-H.; Jiang, J.; Zhang, R.; Wang, Y.; Wan, G.; Siriviboon, P.; Yoon, M.; Ye, P. D.; Wu, W.; Li, M.; Huang, S. Thickness-Dependent Polaron Crossover in Tellurene. *Sci. Adv.* **2025**, *11* (2),

eads4763. <https://doi.org/10.1126/sciadv.ads4763>.

- (75) Hruska, E.; Husek, J.; Bandaranayake, S.; Baker, L. R. Visible Light Absorption and Hot Carrier Trapping in Anatase TiO₂: The Role of Surface Oxygen Vacancies. *J. Phys. Chem. C* **2022**, *126* (26), 10752–10761. <https://doi.org/10.1021/acs.jpcc.2c02978>.
- (76) Redondo, J.; Reticcioli, M.; Gabriel, V.; Wrana, D.; Ellinger, F.; Riva, M.; Franceschi, G.; Rheinfrank, E.; Sokolović, I.; Jakub, Z.; Kraushofer, F.; Alexander, A.; Belas, E.; Patera, L. L.; Repp, J.; Schmid, M.; Diebold, U.; Parkinson, G. S.; Franchini, C.; Kocan, P.; Setvin, M. Real-Space Investigation of Polarons in Hematite Fe₂O₃. *Sci. Adv.* **2024**, *10* (44), eadp7833. <https://doi.org/10.1126/sciadv.adp7833>.
- (77) Alexandrov, V.; Rosso, K. M. Electron Transport in Pure and Substituted Iron Oxyhydroxides by Small-Polaron Migration. *J. Chem. Phys.* **2014**, *140* (23), 234701. <https://doi.org/10.1063/1.4882065>.
- (78) Li, H.; Zhou, Z.; Vasenko, A. S.; Chulkov, E. V.; Fang, Q.; Long, R. Formation and Recombination Dynamics of Polarons in Goethite: A Time-Domain Ab Initio Study. *J. Phys. Chem. Lett.* **2024**, *15* (39), 10018–10025. <https://doi.org/10.1021/acs.jpclett.4c02493>.
- (79) Wu, H.; Zhang, L.; Qu, S.; Du, A.; Tang, J.; Ng, Y. H. Polaron-Mediated Transport in BiVO₄ Photoanodes for Solar Water Oxidation. *ACS Energy Lett.* **2023**, *8* (5), 2177–2184. <https://doi.org/10.1021/acsenergylett.3c00465>.
- (80) Kweon, K. E.; Hwang, G. S. Structural Phase-Dependent Hole Localization and Transport in Bismuth Vanadate. *Phys. Rev. B* **2013**, 205202. <https://doi.org/10.1103/PhysRevB.87.205202>.
- (81) Alam, M.; Mandal, K. Origin of Ferroelectricity in Multiferroic ErFeO₃. *Phys. B Condens. Matter* **2021**, *612*, 412935. <https://doi.org/10.1016/j.physb.2021.412935>.
- (82) Macridin, A.; Sawatzky, G. A.; Jarrell, M. Two-Dimensional Hubbard-Holstein Bipolaron. *Phys. Rev. B* **2004**, *69* (24), 245111. <https://doi.org/10.1103/PhysRevB.69.245111>.
- (83) Nosarzewski, B.; Huang, E. W.; Dee, P. M.; Esterlis, I.; Moritz, B.; Kivelson, S. A.; Johnston, S.; Devereaux, T. P. Superconductivity, Charge Density Waves, and Bipolarons in the Holstein Model. *Phys. Rev. B* **2021**, *103* (23), 235156. <https://doi.org/10.1103/PhysRevB.103.235156>.
- (84) Bonča, J.; Trugman, S. A. Bipolarons in the Extended Holstein Hubbard Model. *Phys. Rev. B* **2001**, *64* (9), 094507. <https://doi.org/10.1103/PhysRevB.64.094507>.
- (85) De Filippis, G.; Cataudella, V.; Iadonisi, G.; Marigliano Ramaglia, V.; Perroni, C. A.; Ventriglia, F. Polaron and Bipolaron Formation in the Hubbard-Holstein Model: Role of next-Nearest-Neighbor Electron Hopping. *Phys. Rev. B* **2001**, *64* (15), 155105. <https://doi.org/10.1103/PhysRevB.64.155105>.
- (86) Fehske, H.; Roder, H.; Mistriots, A.; Buttner, H. The Phase Diagram of the 2D Holstein-t-J Model near Half Filling. *J. Phys. Condens. Matter* **1993**, *5* (22), 3565. <https://doi.org/10.1088/0953-8984/5/22/008>.
- (87) Ji, G.; Xu, M.; Kendrick, L. H.; Chiu, C. S.; Brüggenjürgen, J. C.; Greif, D.; Bohrdt, A.; Grusdt, F.; Demler, E.; Lebrat, M.; Greiner, M. Coupling a Mobile Hole to an Antiferromagnetic Spin Background: Transient Dynamics of a Magnetic Polaron. *Phys. Rev. X* **2021**, *11* (2), 021022. <https://doi.org/10.1103/PhysRevX.11.021022>.
- (88) Davydova, M.; Zhang, Y.; Fu, L. Itinerant Spin Polaron and Metallic Ferromagnetism in Semiconductor Moiré Superlattices. *Phys. Rev. B* **2023**, *107* (22), 224420. <https://doi.org/10.1103/PhysRevB.107.224420>.

Supporting Information for:

**Experimentally Mapping the Phase Diagrams of Photoexcited Small
Polarons**

Jocelyn L. Mendes and Scott K. Cushing*

Division of Chemistry and Chemical Engineering, California Institute of Technology, Pasadena,
California 91125, United States

*Correspondence and requests for materials should be addressed to S.K.C. (email: scushing@caltech.edu)

Supporting Information Contents

S1. Experimental Setup: Transient Extreme Ultraviolet Reflectivity Spectrometer.....	16
S2. Fe ₂ SiO ₄ Spectral Analysis.....	16
References	17

S1. Experimental Setup: Transient Extreme Ultraviolet Reflectivity Spectrometer

Here we describe the experimental methods used to measure the Fe₂SiO₄ samples. The transient extreme ultraviolet (XUV) reflectivity spectrometer is described previously.^{S1,S2} A Legend Elite Duo laser system (Coherent Inc.) with 35 fs, 13 mJ, 1 kHz pulses centered at 800 nm is split by a 75:25 beam splitter with ~10 mJ used for the pump path and ~3 mJ being used to generate a few-cycle white light beam (<6 fs, 550-900 nm) for high harmonic generation (HHG). The pump path uses the 400 nm frequency doubled output of a BBO crystal with p-polarization, pumped with the 800 nm output of the Ti:Sapphire laser. The optical excitation fluence used in the Fe₂SiO₄ measurements was ~14 mJ/cm². Transient reflection is measured at a 10° grazing incidence (80° from normal incidence) geometry and measures the varying delay times between the pump and probe pulses by an optomechanical delay stage. The photoexcited dynamics were probed with an XUV pulse produced with an s-polarized few-cycle white light pulse by HHG in argon. The residual white light beam is removed with a 200 nm thick Al filter (Luxel). The generated XUV continuum is used to probe the Fe M_{2,3} absorption edges at ~54 eV. An edge-pixel referencing scheme was used to denoise the spectra due to intensity fluctuations and used signal-free spectral regions.^{S3}

S2. Fe₂SiO₄ Spectral Analysis

Transient XUV reflection spectroscopy measures the photoexcited polaron formation dynamics of Fe₂SiO₄ following photoexcitation with a 3.1 eV (400 nm) pump beam. Measurements result in surface sensitive spectra, with a probe penetration depth of ~2 nm. The differential reflection-absorption following photoexcitation is defined as $\Delta\text{OD} = -\log_{10}(I_{\text{pump on}}/I_{\text{pump off}})$.

Figure S1A shows a representative transient spectrum of Fe₂SiO₄ measured at the Fe M_{2,3} X-ray edge. Immediately following photoexcitation, there is an increase in absorption at ~53.0 – 54.0 eV (red feature) and a neighboring decrease in absorption from ~54.0 – 55.8 eV (blue feature). The transient features experience a blue shift that begins immediately after photoexcitation, and this spectral shift is complete after ~200 fs. Figure S1B demonstrates lineouts from the transient spectra immediately following photoexcitation (blue) and 1 ps after photoexcitation (green) when the spectral shift is complete. We attribute the blue lineout in Figure S1B to the charge transfer state immediately following photoexcitation. We assign the green lineout in Figure S1B to the photoexcited polaron state. A fitting of the spectral blueshift associated with the polaron formation (Fig. S1C) results in a shift with a magnitude of 460 ± 90 eV and a time constant of 130 ± 40 fs.

We further conduct singular value decomposition (SVD) to extract the contributions of the charge transfer and polaronic states to the spectrum at different timepoints. Figure S1D shows the SVD of the Fe₂SiO₄ spectrum and demonstrates a transition from the charge transfer state to the polaron state that occurs in 10s of fs.

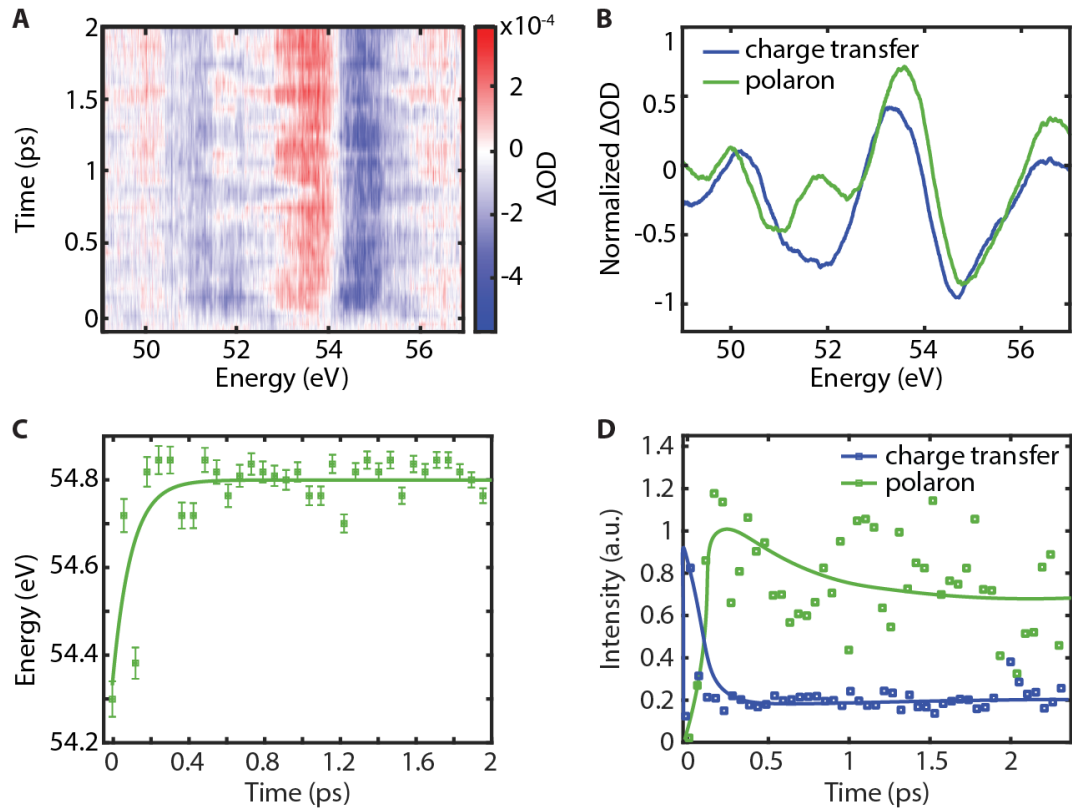


Figure S1. Representative transient XUV spectrum at the Fe M_{2,3} edge centered at ~54 eV (**A**). Spectral lineouts 30 fs (blue) and 1 ps (green) after photoexcitation with a 400 nm pump (**B**), where the lineout at 30 fs is attributed to the charge transfer state and the lineout at 1 ps is attributed to the polaron state. A fitting of the spectra blueshift at the Fe M_{2,3} edge (**C**), taken by averaging the signal at the blue feature in (**A**) from ~54.0 – 55.0 eV, reveals that polaron formation occurs with a time constant of 130 ± 40 fs. Singular value decomposition (**D**) of the charge transfer (blue) and polaron (green) states from (**B**) where the charge transfer state begins to transition to the polaron state within 10s of fs.

References

- (1) Kim, Y.-J.; Mendes, J. L.; Michelsen, J. M.; Shin, H. J.; Lee, N.; Choi, Y. J.; Cushing, S. K. Coherent Charge Hopping Suppresses Photoexcited Small Polarons in ErFeO₃ by Antiadiabatic Formation Mechanism. *Sci. Adv.* **2024**, *10* (12), eadk4282. <https://doi.org/10.1126/sciadv.adk4282>.
- (2) Liu, H.; Michelsen, J. M.; Mendes, J. L.; Klein, I. M.; Bauers, S. R.; Evans, J. M.; Zakutayev, A.; Cushing, S. K. Measuring Photoexcited Electron and Hole Dynamics in ZnTe and Modeling Excited State Core-Valence Effects in Transient Extreme Ultraviolet Reflection Spectroscopy. *J. Phys. Chem. Lett.* **2023**, 2106–2111. <https://doi.org/10.1021/acs.jpclett.2c03894>.
- (3) Géneaux, R.; Chang, H.-T.; Schwartzberg, A. M.; Marroux, H. J. B. Source Noise Suppression in Attosecond Transient Absorption Spectroscopy by Edge-Pixel Referencing. *Opt. Express* **2021**, *29* (2), 951. <https://doi.org/10.1364/OE.412117>.